



S62 on a 9.9 yr Orbit around SgrA*

Florian Peißker¹ , Andreas Eckart^{1,2} , and Marzieh Parsa¹¹Physikalisches Institut der Universität zu Köln, Zùlpicher Str. 77, D-50937 Köln, Germany; peissker@ph1.uni-koeln.de²Max-Planck-Institut für Radioastronomie, Auf dem Hùgel 69, D-53121 Bonn, Germany

Received 2019 July 18; revised 2019 November 21; accepted 2019 November 22; published 2020 January 24

Abstract

We present the Keplerian orbit of S62 around the supermassive black hole Sagittarius A* (SgrA*) in the center of our Galaxy. We monitor this S-star cluster member over more than a full orbit around SgrA* using the Very Large Telescope with the near-infrared instruments Spectrograph for INtegral Field Observations in the Near Infrared (SINFONI) and NAOS+CONICA (NACO). For that, we are deriving positional information from deconvolved images. We apply the Lucy–Richardson algorithm to the data sets. The NACO observations cover data from 2002 to 2018, and the SINFONI data cover 2008–2012. S62 can be traced reliably in both data sets. Additionally, we adapt one KECK data point for 2019 that supports the reidentification of S62 after the pericenter passage of S2. With $t_{\text{period}} = 9.9$ yr and a periaapse velocity of approximately 10% of the speed of light, S62 has the shortest known stable orbit around the supermassive black hole in the center of our Galaxy to date. From the analysis, we also derive the enclosed mass from a maximum likelihood method to be $4.15 \pm 0.6 \times 10^6 M_{\odot}$.

Unified Astronomy Thesaurus concepts: Galactic center (565); S stars (1421); Black holes (162)

1. Introduction

With the development of better instrumentation and observational techniques, the immediate environment of the supermassive black hole Sagittarius A* (SgrA*) can be investigated in detail. One of the fundamental quantities that determines the nature of the supermassive black hole SgrA* is its mass. This quantity can be determined using gaseous and stellar probes. An early mass determination was done by Wollman et al. (1977), who found an enclosed mass of $4 \times 10^6 M_{\odot}$ through observations of the $12.8 \mu\text{m}$ Ne II line emission, origination from the mini-spiral located in the Galactic Center stellar cluster. Wollman’s measurements used ionized gas as mass probes. Therefore, it could not be fully excluded that pressure gradients or magnetic fields could have influenced the derived quantity. Also, it was unclear at the time how much the central stellar cluster would contribute to the derived enclosed mass. Therefore, radial velocities (Krabbe et al. 1995) and stellar proper motions of individual stars (Eckart & Genzel 1996, 1997; Ghez et al. 1998) allowed much clearer insight into the amount of compact mass and hence gravitational potential associated with the supermassive black hole SgrA*.

The authors used the Virial theorem and the Jeans equation to derive the distance toward SgrA*. Due to this approach the enclosed mass could only be determined at a minimum distance from SgrA* typically given by the mean separation of the half dozen closest S-stars (see Eckart & Genzel 1997, for the nomenclature). The situation improved when single stars could be used via the detection of curvatures in their orbital tracks (Eckart et al. 2002; Ghez et al. 2002). Complete orbits of the star S2 (Schödel et al. 2002; Eisenhauer et al. 2003; Horrobin et al. 2004; Gillessen et al. 2009b) then allowed measurement of the enclosed mass down to the periaapse distance of this star. Recently, the star S2 could be followed through its periaapse passage using GRAVITY at the VLTI interferometer (Gravity Collaboration et al. 2019). With an orbital analysis of the innermost stars in the S-cluster (the region around SgrA* with a diameter of $1''$, see also Eckart & Genzel 1996), the mass estimate now settled around a value of 4.15 million solar

masses with an uncertainty of about 0.2 million solar masses (Boehle et al. 2016; Parsa et al. 2017; Gravity Collaboration et al. 2019).

The increased precision of the GRAVITY instrument (Gravity Collaboration et al. 2017) allowed a mass determination of $4.148 \pm 0.014 \times 10^6 M_{\odot}$ and a distance of 8175 ± 13 pc. The minimum distance between S2 and SgrA* during the periaapse passage was 17 light hours (120 au) at an orbital period of 16 yr and an ellipticity of 0.88429 ± 0.00006 . Searching for even closer stars resulted in finding the star S0-102 with an 11.2 yr period and an ellipticity of 0.68 ± 0.02 with a correspondingly larger distance from SgrA* (Meyer & Meyer-Hofmeister 2012).

Furthermore, mass probes were possible by investigating hot plasma blobs orbiting the supermassive black hole SgrA*. Here, Karssen et al. (2017) were able to measure the mass enclosed within 15 gravitational radii (R_g ; $1 \sim R_g \sim 5 \mu\text{as} = 0.2 \mu \text{pc}$) by modeling the profiles of the brightest X-ray flares. Tracking hotspots in the near-infrared using the *K*-band interferometric instrument GRAVITY mounted at the VLTI (located in Paranal/Chile, see also Gravity Collaboration et al. 2018a) gave a mass estimate at a distance of only $8 R_g$. It is unclear, how far these estimates derived from ionized hot gas blobs are influenced by viscosity or magnetic fields. Therefore, it would be more effective to use stars that are much closer than the periaapse separation achieved by the star S2 to probe the gravitational potential of SgrA*.

For this work, we will apply the iterative Lucy–Richardson algorithm to our NAOS+CONICA (NACO) and Spectrograph for INtegral Field Observations in the Near Infrared (SINFONI) data. With this high-pass filter, we deblur images and can separate and track stars with high angular resolution. With the results of this analysis technique, we derive the shortest known stable stellar orbit to S62 around SgrA* to date. This star was identified earlier by Gillessen et al. (2009b). We fit a Keplerian orbit to the data and calculate the χ^2 values in order to discuss the quality of the fit. For the orbital fit of S62 around the SMBH in the Galactic center, we use the fitting techniques presented in Parsa et al. (2017). In Section 2, we will explain

SINFONI, K-band, high-pass filtered

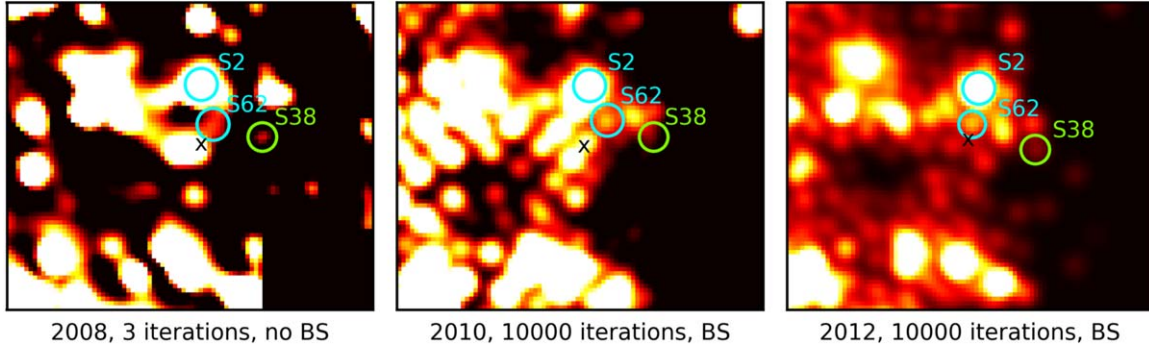


Figure 1. Detection of S62 in the SINFONI data set. The black cross marks the position of SgrA*. S2, S38, and S62 are indicated by circles. North is up and east is to the left. The size of the FOV in all three images is $1''.0 \times 0''.9$. For display purposes, the lookup table is different from image to image. The images before deconvolution are shown in Appendix D.

the observation and the instruments at the VLT. We introduce the applied analysis techniques and discuss the orbit fit. Section 3 presents the results of the analysis and is followed by a discussion, with conclusions in Section 4. In the Appendix, we list the used data, describe the analysis tools in detail, and present the reidentification of S62 during and after the pericenter passage of S2 in 2018.37 (Gravity Collaboration et al. 2019).

2. Observations and Analysis

In this section, we will present the observations that are carried out with the Very Large Telescope in Paranal/Chile. We also give an overview of the data used (see also Appendix A) and introduce the analyzing tools.

2.1. NACO and SINFONI

We are using the near-infrared instrument NAOS+CONICA (NACO) in imaging mode mounted at the VLT (Lenzen et al. 2003; Rousset et al. 2003) with the *K*-band filter. The Adaptive Optics (AO) Laser guide star IRS7 ($\text{mag}_K = 7.7$) is located around $5''.5$ north of SgrA*. The target is randomly dithered within a given area of $4''.0$. Each exposure consists of 3 integrations of 10 s each. The reduction procedure for the data is described in Witzel et al. (2012), Shahzamanian et al. (2016), and Parsa et al. (2017). We use the standard data reduction procedures, including sky subtraction, and bad-pixel and flat-field correction. Parts of the reduced data are also used in Witzel et al. (2012), Eckart et al. (2013), Shahzamanian et al. (2016), and Parsa et al. (2017).

The near-infrared integral field spectrograph SINFONI (Eisenhauer et al. 2003) is, like NACO, mounted at the VLT. The data were downloaded from the ESO archive.³ The data were observed in the H+K grating and with the smallest plate scale of $0''.025$, with an exposure time of 600 s/single observation (see Appendix C). Since the wavefront sensor of SINFONI works only in the optical, the selection for the AO is limited to a star that is located $15''.54$ north and $8''.85$ east of SgrA*. Because the magnitude of the star is at the allowed limit (~ 14 mag), successful observations depend strongly on the weather conditions. To improve the efficiency of the observations, the AO loop could be opened at night to perform reacquisition of the guide star. This would improve the quality

of the data by a factor of 10%–20%. This was done by measuring the PSF of S2 for stable seeing conditions. The sky observations are done on a dark cloud located at $5''.36''$ north and $12''.45''$ west of SgrA*. The B2V star S2 is centered in the upper right quadrant to avoid nonlinear behavior of the detector (see the SINFONI user manual⁴). The standard observational pattern is object (o)—sky (s)—object (o). Every other pattern besides the o-s-o setting influences the data because of the fast sky-variability in the infrared domain during the observations (see Davies 2007; Peißker et al. 2019, for a detailed discussion), and is therefore excluded from the analysis. Standard G2V stars are observed for the telluric correction. We apply a flat-field correction since some slits (usually slit 15 and 16) suffer from increased brightness features. Because the edges of some data cubes show errors that cannot be corrected, we crop these regions by flagging the individual single data cubes.

After the corrections are applied, we select single data cubes with a S2 PSF size of <7.0 pixel in both spatial directions. These selected single cubes are shifted in a 100×100 pixel array to a reference position that is defined from a previous created reference frame. From this, the final data cubes are created from the combination of the corrected single exposures/cubes.

2.2. High-pass Filtering

The Lucy–Richardson algorithm (Richardson 1972; Lucy 1974) can be used to highlight image details. A high-pass filter is one solution to distinguish suppressed signals from emission that is caused by the background as well as the detector. Since the GC is a crowded region with a structured and variable background (Sabha et al. 2012), the deconvolution greatly supports the identification of a distribution of point-like stars. A detailed description is also presented in Peißker et al. (2019). The technique, which derives from Bayes’ theorem on conditional probabilities, conserves the constraints on spatial frequency distributions, and at each iteration increases the likelihood of the resulting deconvolved image representing the observed image. Ott et al. (1999) compared the flux density conserving properties of the Lucy–Richardson, the Clean, and the Wiener deconvolution algorithms for point-like stars in the Galactic Center environment. The robustness of the algorithm is demonstrated in Appendix B. In Figure 1, we present three

³ www.eso.org

⁴ www.eso.org

deconvolved images. We extract K -band images from the collapsed SINFONI data cube (see Figure 11 in Appendix D) and apply, if necessary, a static background subtraction (BS). This BS is adjusted to the data quality, the background of the object, and the detector noise. Because of unavoidable superposition effects in the crowded GC regarding the PSF, we are using an artificial PSF (APSF). This APSF is created and modified with respect to the observed “natural” PSF of S2, the brightest source in the SINFONI field of view (FOV). In general, the SINFONI PSF is often rotated and shows an elongated shape with short and long axis values between 4 and 7 px depending on the data quality. The quality of the deconvolved images depends on the match of the APSF to the real PSF and the correct choice of the BS. A large number of iterations is required to allow the algorithm to converge to a stable solution at all flux density levels. The effect can be seen in Figure 1. The robustness of the S62 source detection in the framework of artificial source planting and PSF subtraction is discussed in Appendices B and E.

2.3. Orbital Fit

For the orbital fit of S62, stellar positions for each epoch of observation are measured using the NACO data and QFitsView (Thomas Ott, MPE Garching). The position of SgrA* in the NACO data is based on the well-known orbit of S2 (see Gillessen et al. 2009a, 2017; Parsa et al. 2017) in combination with the orbital elements. Based on the orbit and the offset positions of S2, we can determine the position of SgrA* (Parsa et al. 2017; Gravity Collaboration et al. 2019) in order to create the reference frame. From this, we extract the offset position of S62 to SgrA*. This procedure can be also applied to the SINFONI data. The position of SgrA* is consistent with observed flares in the $H+K$ -band and the SiO masers.

For the Keplerian fit, we are using the minimizing and iterative method L-BFGS-B (see e.g., Saputro & Widyandingsih 2017) for handling the bound constraints. This memory-friendly algorithm is suitable for box constraints. We fit the semimajor axis, the eccentricity, the inclination, the periapsis, the longitude, and the time for the closest approach with respect to the starting time of the algorithm.

We obtained a starting value (initial guess) for the orbital elements by varying the R.A. and decl. values of the measured positions by ± 6.5 mas, averaging the results, and determined the 1σ uncertainties. Then we allowed the elements to vary randomly within their 3σ limits. We bootstrapped the solution using 50 representations of the randomized elements calculating the resulting orbits and the deviation from the measured data. Following this approach, we obtained the best-fitting orbit and the uncertainties from the uncertainty-weighted distribution of the orbital elements.

From Gravity Collaboration et al. (2019), we use a mass for SgrA* of $4.15 \times 10^6 M_{\odot}$. Because we are using stellar offset positions, the location of the SMBH is centered in the origin of the reference frame. Due to variations in the line-of-sight background of the S-stars and its relative position with respect to bright neighboring sources, the stellar positions measured from single-epoch images do not necessarily show a Gaussian distribution. For each year, we are therefore using the median position⁵ of S62 whenever possible. With this approach, we

⁵ The median is less sensitive to outliers and in case of a Gaussian distribution the median equals the mean.

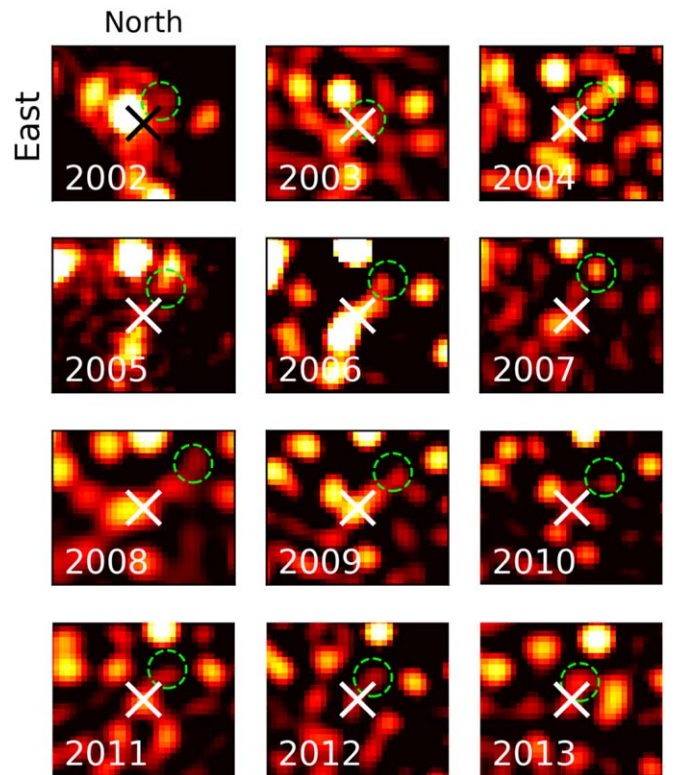


Figure 2. Selected overview of the S62 position in the NACO data around SgrA* between 2002 and 2013. The white cross indicates the position of SgrA*; S62 is located at the position of the lime dashed circle. The images are centered on SgrA*. The size of the FOV is $0''.42 \times 0''.36$. The angular resolution of the images is at the 60 mas diffraction limit of the telescope in the K band. For the reidentification of S62 after the S2 passage through the field of view in 2014–2016 see Appendix C.

minimize the effect of outlying data points and pay tribute to the variable background (see also simulations by Sabha et al. 2012 and the Appendices B and C in this work).

3. Results

In this section, we will show the results of our Keplerian fit and the enclosed mass of SgrA*. From the NACO and SINFONI images, we derive the distance between SgrA* and S62 for every analyzed data set. They are based on deconvolved K - & $H+K$ band images. The Keplerian fit results in a 9.9 yr orbit of S62 around SgrA* (Figure 2) and is based on the NACO detection and the KECK data point adapted from Do et al. (2019; see also Appendix C). The resulting orbital parameters can be found in Table 1. To underline the robustness of the fit, we include the SINFONI data (red data points) of 2008, 2010, and 2012.

3.1. Orbit

We derive a highly eccentric orbit with an eccentricity of $e = 0.976 \pm 0.002$. We also find the closest point of S62 to SgrA* with ~ 2 mas. This corresponds to around $215 R_s$.

Since the first observed periapse of S2 in 2002, the orbit of S62 can be observed and analyzed. With a K -band magnitude of around ~ 14 mag, S2 is the brightest member of the S-cluster. Stars, that have positions close to S2, are therefore blended. Because S62 is on a highly eccentric 9.9 yr orbit, the observations after 2013 show overlap with the S2 orbit (see Figures 3 and 4). It can be concluded that S62 is only observable without blending

Table 1
Orbital Parameters for S62 (The 1σ Uncertainty is Based on the Variation of R.A. and Decl. Values by ± 6.5 Mas)

Source	a (mpc)	e	i ($^\circ$)	ω ($^\circ$)	Ω ($^\circ$)	t_{closest} (yr)	t_{period} (yr)
S62	3.588 ± 0.002	0.976 ± 0.002	72.76 ± 4.58	42.62 ± 0.4	122.61 ± 0.57	2003.33 ± 0.01	9.9 ± 0.02

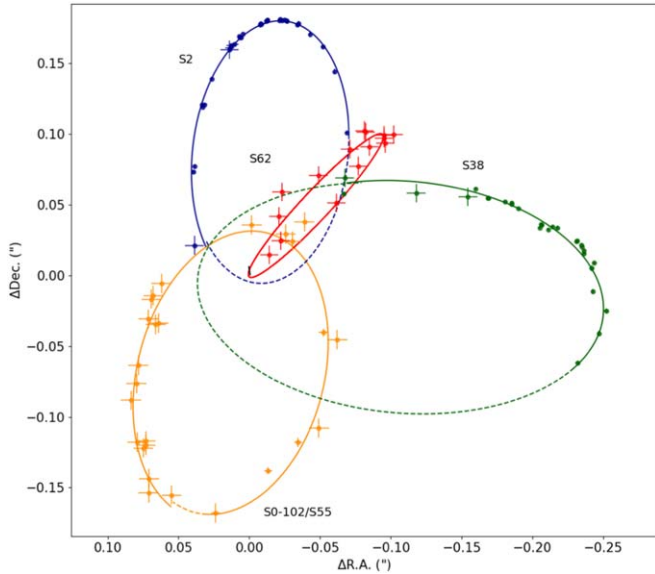


Figure 3. Orbit overview of S2, S38, S62, and S0-102. SgrA* is located at the origin of the coordinate system. See also Figure 3 in Parsa et al. (2017).

after the periape of S2 in a time period for around 11 yr (see Figure 5). This is sufficient to cover one full orbit of the S-star S62. To highlight the robustness of the fit, Figure 6 shows the residual plot of the orbital fit. The error bars (about ± 0.5 px = ± 6.5 mas) are adapted from the positional uncertainty (see uncertainties in Table 2) of the orbit plot. The standard deviation for the R.A. plot is 3.75 mas and that for the decl. plot is 8.59 mas and therefore in good agreement with the positional error of ± 6.5 mas.

3.2. Minimized Likelihood

The minimize function for the six orbital elements as a function of the mass of SgrA* returns the residuals squared of the (initial guess) parameters. The likelihood function can be interpreted as an indicator for the goodness of the fit (Parsa et al. 2017), since it calculates the sum of the squared residuals. From the minimized and optimized orbital fit parameters, we are introducing a variation of the SMBH mass. Based on the analysis and the fit, the resulting plot of the likelihood function as a function of the mass of SgrA* is showing a minimum at $(4.15 \pm 0.6) \times 10^6 M_\odot$, which is consistent with the mass derived by Gravity Collaboration et al. (2019). The uncertainties of the mass are derived from the range of mass values for which the variation of the value of the χ^2 value is below unity. Hence, we find for the central mass $(4.15 \pm 0.6) \times 10^6 M_\odot$ (see Figure 7). This value is in good agreement with the mass derived by Gravity Collaboration et al. (2018a, 2018b, 2019).

3.3. Enclosed Mass

As described in Section 3.2, we find a maximum for the minimize function that defines the enclosed mass. This value is

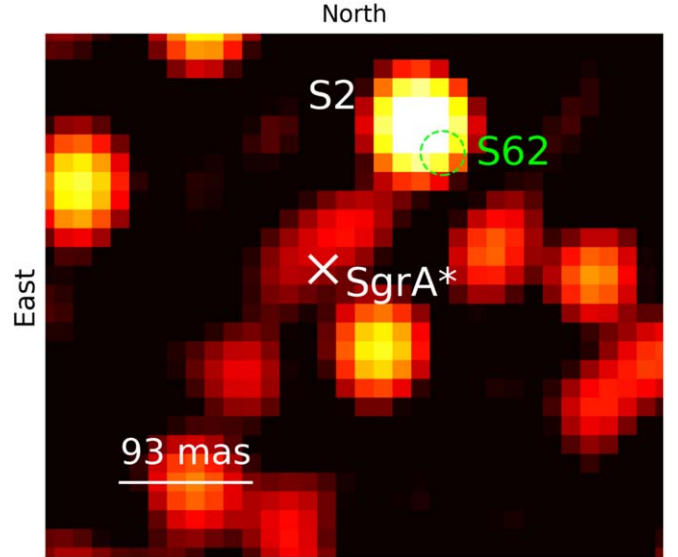


Figure 4. The GC in 2015. SgrA* is located at the white cross, and S62 is expected to be at the location indicated by a lime dashed circle. S62 is too close to S2 and therefore not observable.

based on a identification that marks the closest observed separation from a stellar source on a stable orbit to a supermassive black hole to date. S62 is located significantly closer to the SMBH than to S2 (see Gillessen et al. 2017, 2009a; Parsa et al. 2017) or S0-102 (Meyer & Meyer-Hofmeister 2012). We can compare our result with other known objects in the GC (see Figure 8). The hotspot estimation as well as the error are based on the modeling of Karssen et al. (2017). The authors use scale-free orbiting hotspot modeling that is based on the shape of observed flares. From this, they derive the mass of the central black hole associated with SgrA* after introducing the observed flare length in seconds. The authors find a value of $3.9_{-1.8}^{+4.8} \times 10^6 M_\odot$ enclosed within $15 R_g$, i.e., 7.5 Schwarzschild radii ($3.0 \mu\text{pc}$). Gravity Collaboration et al. (2019) observed infrared hotspots orbiting SgrA* at a separation of 6–10 R_g , i.e., 3–5 Schwarzschild radii (1.2 – $2 \mu\text{pc}$). Based on the GRAVITY observations, the authors of Gravity Collaboration et al. (2019) derive an enclosed mass of $4.15 \pm 0.01 \times 10^6 M_\odot$. The values for the CND, S2, Stellar disk, and late-type stars in Figure 8 are adopted from Genzel et al. (2010).

4. Discussion and Conclusion

This section summarizes the findings. We will discuss the results and give an brief outlook to upcoming observations. We also compare S62 to the hotspot model.

4.1. Properties of S62

We compare the peak counts of S2 and S62 in 2012 with a one-pixel aperture. From this, we find a factor of 6 between

Table 2
Stellar Positions of S62 for Our SINFONI and NACO Data

Date	NACO		SINFONI		KECK	
	$\Delta R.A.$ (mas)	$\Delta Decl.$ (mas)	$\Delta R.A.$ (mas)	$\Delta Decl.$ (mas)	$\Delta R.A.$ (mas)	$\Delta Decl.$ (mas)
2002.57	-22.35 ± 5.64	24.37 ± 5.51
2003.44	-14.04 ± 4.77	14.56 ± 5.21
2004.51	-61.32 ± 4.42	51.38 ± 4.92
2005.42	-77.09 ± 5.04	77.41 ± 5.62
2006.72	-102.05 ± 3.99	99.71 ± 4.66
2007.25	-96.00 ± 5.64	93.40 ± 5.51
2008.26	-92.50 ± 5.5	95.00 ± 8.5
2008.36	-95.09 ± 4.77	97.11 ± 5.21
2009.50	-95.03 ± 5.64	99.02 ± 5.51
2010.36	-70.80 ± 4.77	89.50 ± 5.21	-88.12 ± 4.6	92.50 ± 7.2
2011.34	-48.77 ± 4.42	70.92 ± 4.92
2012.37	-22.92 ± 5.64	59.11 ± 5.51
2012.49	-27.50 ± 3.4	65.00 ± 5.45
2013.49	-20.74 ± 4.77	41.89 ± 5.21
2017.50	-81.38 ± 2.16	102.44 ± 3.23
2018.35	-84.89 ± 1.33	90.87 ± 1.20
2019.37	—	...	-82.27 ± 5.00	101.26 ± 5.00

Note. The uncertainties for the NACO and SINFONI data are based on the Gaussian fit of the source itself and equals an average of about ± 0.5 pixels corresponding to 6.25 mas (SINFONI) and 6.5 mas (NACO). For the data point in 2019, we also make use of one KECK data point presented in Do et al. (2019, Figure 1). Consistent with our NACO and SINFONI data, we adopted a positional uncertainty of ± 5 mas in each direction.

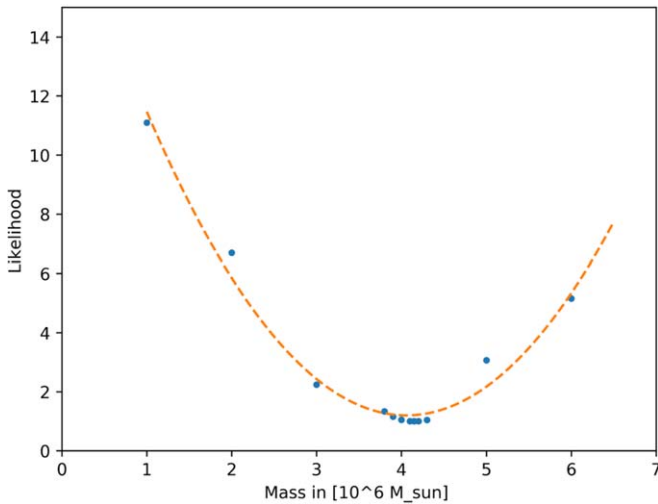


Figure 7. Likelihood as a function of mass. We normalized the resulting likelihood fit values to the minimum value of the mass variation analysis.

Assuming a mass of $2.2 M_{\odot}$ for S62 (see above), we find $R_* = 2.06 R_{\odot}$ and a tidal disruption radius of $251 R_{\odot}$ or 1.18 au. This can be compared to the periape separation r_p . Using the orbital elements in Table 1 we find

$$r_p = a(1 - e) \approx 16 \text{ au.} \quad (5)$$

Hence, the periape distance of S62 is about 3 times the hotspot distance as determined by Karssen et al. (2017) and just about 15 times the tidal disruption radius. Certainly, tidal interactions will already be important for the evolution of S62. The derived and observed properties of S62 indicate that it is indeed an S-star member on a tight orbit around the supermassive black hole SgrA*.

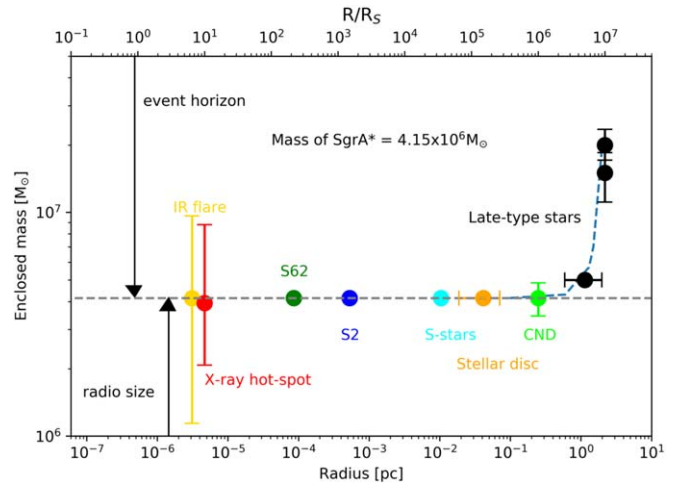


Figure 8. Enclosed mass of several objects. The first vertical dashed line marks the event horizon of SgrA*, and the second one marks the measured radio size of the black hole. The uncertainties of the X-ray hotspot are based on Karssen et al. (2017). If no error bar is shown, the uncertainty of the mass determination is at or below the thickness of the symbol. The IR-flare error is at $4.14_{-1.14}^{+1.36} \times 10^6 M_{\odot}$ (Gravity Collaboration et al. 2018b). See also Figure 5.1.1 in Genzel et al. (2010).

4.2. Gravitational Periape Shift

We determine a minimum distance of S62 to SgrA* that is comparable to about 30 times the distance determined with the hotspot model presented by Karssen et al. (2017). Figure 8 shows that S62 is an excellent candidate to show relativistic effects presented in Parsa et al. (2017) and Gravity Collaboration et al. (2018a, 2019). Since the orbital timescale is measured to be 9.9 yr, the next pericenter passage will be around 2023 March.

During that passage, the star will have a velocity of about 10% the speed of light.

All experiments indicate that the mass associated with SgrA* is very compact and is most likely presented in the form of a supermassive black hole (Eckart et al. 2017). In this case, the relativistic *prograde* pericenter advance per revolution is given by (see Weinberg 1972, Equation (8.6.11))

$$\Delta\varphi = \frac{6\pi G}{c^2} \frac{M}{a(1 - e^2)}, \quad (6)$$

with a being the semimajor axis and e being the eccentricity of the orbit.

Using the values from the orbital elements for S62, we find a periaapse advance of 9°9. Given the value of the argument of the pericenter ω , a significant fraction of the periaapse advance should be measurable on the sky. Since a full orbit tracking would be out of phase with S2 probably every second orbit of S62, the star can be observed and used to derive the periaapse advance.

The expected shifts in position due to the relativistic periastron shift are currently well within the positional uncertainties of our

measurements. However, future interferometric observations with GRAVITY will considerably improve the results.

We are grateful to Basel Ali (I. Physikalisches Institut, Cologne) for support with the source identification and the related orbit calculations. We also thank the members of the NACO/SINFONI and ESO Paranal/Chile team. This work was supported in part by the Deutsche Forschungsgemeinschaft (DFG) via the Cologne Bonn Graduate School (BCGS), the Max Planck Society through the International Max Planck Research School (IMPRS) for Astronomy and Astrophysics, as well as special funds through the University of Cologne and SFB 956: Conditions and Impact of Star Formation. We thank the Collaborative Research Centre 956, sub-project [A02], funded by the Deutsche Forschungsgemeinschaft (DFG) project ID 184018867.

Appendix A Data

In Tables 3 and 4, we give an overview of the used NACO data. Table 5 shows the analyzed SINFONI data.

Table 3
First Part of the K-band NACO Data

NACO				
Date (UT)	Observation ID	Number of Exposures	Total Exposure Time(s)	λ
2002 Jul 31	60.A-9026(A)	61	915	K
2003 Jul 13	713-0078(A)	253	276.64	K
2004 Jul 6	073.B-0775(A)	344	308.04	K
2004 Jul 8	073.B-0775(A)	285	255.82	K
2005 Jul 25	271.B-5019(A)	330	343.76	K
2005 Jul 27	075.B-0093(C)	158	291.09	K
2005 Jul 29	075.B-0093(C)	101	151.74	K
2005 Jul 30	075.B-0093(C)	187	254.07	K
2005 Jul 30	075.B-0093(C)	266	468.50	K
2005 Aug 2	075.B-0093(C)	80	155.77	K
2006 Aug 2	077.B-0014(D)	48	55.36	K
2006 Sep 23	077.B-0014(F)	48	55.15	K
2006 Sep 24	077.B-0014(F)	53	65.10	K
2006 Oct 3	077.B-0014(F)	48	53.84	K
2006 Oct 20	078.B-0136(A)	47	42.79	K
2007 Mar 4	078.B-0136(B)	48	39.86	K
2007 Mar 20	078.B-0136(B)	96	76.19	K
2007 Apr 4	179.B-0261(A)	63	49.87	K
2007 May 15	079.B-0018(A)	116	181.88	K
2008 Feb 23	179.B-0261(L)	72	86.11	K
2008 Mar 13	179.B-0261(L)	96	71.49	K
2008 Apr 8	179.B-0261(M)	96	71.98	K
2009 Apr 21	178.B-0261(W)	96	74.19	K
2009 May 3	183.B-0100(G)	144	121.73	K
2009 May 16	183.B-0100(G)	78	82.80	K
2009 Jul 3	183.B-0100(D)	80	63.71	K
2009 Jul 4	183.B-0100(D)	80	69.72	K
2009 Jul 5	183.B-0100(D)	139	110.40	K
2009 Jul 5	183.B-0100(D)	224	144.77	K
2009 Jul 6	183.B-0100(D)	56	53.81	K
2009 Jul 6	183.B-0100(D)	104	72.55	K
2009 Aug 10	183.B-0100(I)	62	48.11	K
2009 Aug 12	183.B-0100(I)	101	77.32	K

Note. For every epoch, the number of exposures used for the final mosaics, the total exposure time, and the Project ID are listed. Note that NACO was decommissioned between 2013 and 2015.

Table 4
Second Part of the *K*-band NACO Data

NACO					
Date(UT)	Observation ID	Number of Exposures	Total Exposure Time(s)		λ
2010 Mar 29	183.B-0100(L)	96	74.13		K
2010 May 9	183.B-0100(T)	12	16.63		K
2010 May 9	183.B-0100(T)	24	42.13		K
2010 Jun 12	183.B-0100(T)	24	47.45		K
2010 Jun 16	183.B-0100(U)	48	97.78		K
2011 May 27	087.B-0017(A)	305	4575		K
2012 May 17	089.B-0145(A)	169	2525		K
2013 Jun 28	091.B-0183(A)	112	1680		K
2017 Jun 16	598.B-0043(L)	36	144		K
2018 Apr 24	101.B-0052(B)	120	1200		K

Table 5
SINFONI Data of 2008, 2010, and 2012

SINFONI							
Date	Observation ID	Start Time	End Time	Amount and Quality of the Data			Exp. Time
				Total	Medium	High	
(YYYY:MM:DD)		(UT)	(UT)				(s)
2008 Apr 6	081.B-0568(A)	05:25:26	08:50:00	16	0	15	600
2008 Apr 7	081.B-0568(A)	08:33:58	09:41:05	4	0	4	600
2010 May 10	183.B-0100(O)	06:03:00	09:35:20	3	0	3	600
2010 May 11	183.B-0100(O)	03:58:08	07:35:12	5	0	5	600
2010 May 12	183.B-0100(O)	09:41:41	09:57:17	13	0	13	600
2012 Mar 18	288.B-5040(A)	08:55:49	09:17:01	2	0	2	600
2012 May 5	087.B-0117(J)	08:09:14	08:41:33	3	0	3	600
2012 May 20	087.B-0117(J)	08:13:44	08:23:44	1	0	1	600
2012 Jun 30	288.B-5040(A)	01:40:19	06:54:41	12	0	10	600
2012 Jul 1	288.B-5040(A)	03:11:53	05:13:45	4	0	4	600
2012 Jul 8	288.B-5040(A)/089.B-0162(I)	00:47:39	05:38:16	13	3	8	600
2012 Sep 8	087.B-0117(J)	00:01:36	00:23:33	2	1	1	600
2012 Sep 14	087.B-0117(J)	01:21:30	01:43:27	2	0	2	600

Note. For an overview, the total amount of data in the related years is listed. To ensure the best signal-to-noise ratio for our combined final data cubes, we are just using single data cubes with high quality. Dates are listed in UT.

Appendix B Source Crowding and Noise

Since the Galactic center is a very crowded region, we need to investigate how far our source identifications are compromised by the crowding effects. In the following, we investigate the detection of sources in a crowded field, the influence of excess pixel noise on the deconvolution, and the probability of finding a serendipitous orbit.

Source detection in a crowded field: in order to test the liability of our source detection, we conducted source planting experiments. We created a 4×4 array of artificial sources with the same noise and flux properties as S62. We added this to individual images before deconvolution. After deconvolution, we tested if the artificially placed sources could be detected. We randomly positioned the 4×4 array on several images and repeated the process. The result of the investigation in the image can be divided into three different zones (see Figure 9):

Zone I: artificially planted sources that are within a radius of 0.3 times the half-power width of detected (real) S-stars could

not be separated from the objects originally presented in the image. In this case, the sources within Zone I had a flux corresponding to the one from the planted source plus the flux of the original source at that position after the deconvolution. *Zone II:* for a small region with a distance of 0.3–0.6 times the half-power width from an S-star, we could retrieve about 60% of the planted sources with mostly compromised positions and fluxes. Those position measurements, which may have been influenced by neighboring sources in Zone II, are suppressed as extreme values by choosing the median in order to combine the different stellar positions per epoch.

Zone III: for the entire region with separations of at least 0.6 times the half-power width of detected sources, we could always separate the planted sources from the sources presented in the image. Since the angular velocity of S62 in the crowded lower half part of its orbit is well above 30 mas yr^{-1} , the chances of finding it in Zone I for the duration of an entire year are very small. Combined with the fact that we discarded source detections with fluxes significantly larger than the S62

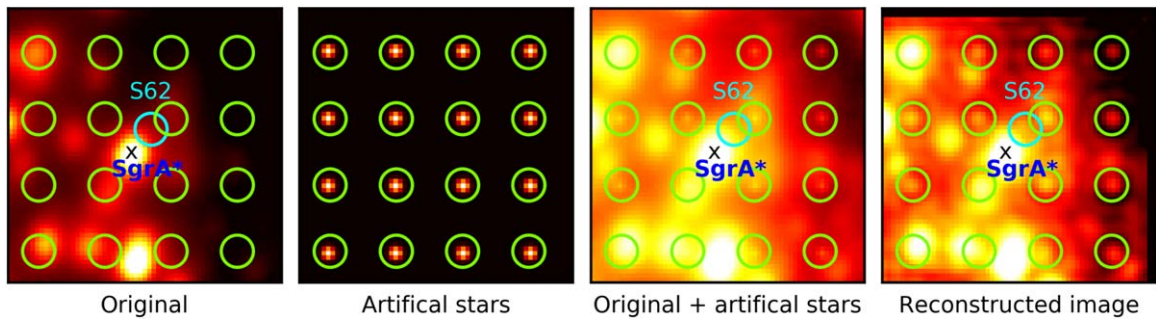


Figure 9. Example from the test on one particular field: (a) original image; (b) array of artificial stars, counting from top left (1) to bottom right (16); (c) original image with artificial stars planted; (d) result after deconvolution and reconvolving to the final angular resolution close to the diffraction limit. Zone I cases: the artificial sources at field positions 1 and 13 could not be separated from the natural star close to those positions. Zone II cases: at field positions 7 and 14, the planted artificial star can be identified but is close to a natural star. Zone III cases: in all other field positions, the planted artificial stars fell at or beyond half a PSF width from a natural star and could clearly be separated.

flux, our source detections are all located exclusively in Zone III. However, depending on the time variable (since everything is moving), the local line-of-sight background, and the distribution of brighter sources close to the line of sight (and corresponding gradients in the local background), the positional uncertainty may reach ± 10 mas (i.e., about a sixth of a beam) for the median of several position estimates. This uncertainty may be higher for individual single-epoch images (see simulations by Sabha et al. 2012 and Eckart et al. 2013). The authors derive the chance for a false-positive detection of a few percent for sources, which are detected for three consecutive years. We can conclude from this analysis, that the uncertainty for detecting a false-positive detection is significantly smaller than 1% since we detect S62 for 11 consecutive years.

Influence of noise: all images had an exposure time sufficient to detect the source. The S-cluster was always positioned in regions of the detector array with extremely good cosmetics. There were no regions of defective pixels, which are close in size to the PSF. The likelihood of individually healthy pixels forming a simultaneous positive fluctuation is proportional to σ^N , where N is the number of pixels characteristic of the size of a PSF. This is very unlikely to happen. For 1σ and $N = 10$, the likelihood is already only $\times 10^{-5}$.

The effect of single pixels with a statistically high count rate should also be discussed. The influence of single-pixel excursions is strongly suppressed by the Lucy algorithm. The reason is that the ratio of images to correct the $(i - 1)$ th iteration in order to obtain the new i th iteration is convolved with the PSF (see Equation (15) in Lucy 1974). Therefore, the effect of a single pixel is smeared out over the entire PSF. We did experiments with 5σ – 8σ excursions in the count rate and did not find any significant effects in the resulting deconvolved images. Only if the flux in a single affected pixel approaches a good portion of the flux contained in the faintest detected sources might they become a source of confusion. In our images, we did not find an excessive count-rate excursion of single pixels that would have led to such an effect.

Probability of finding an serendipitous orbit: one may find indications for orbital motion if sources of a suitable magnitude serendipitously occur close to the investigated orbital positions. There are about 50 sources within the central arcsecond that are bright enough to derive and trace their orbit. Only a fraction of them have a flux density compatible with S62. If we require the

source to be identified within a single PSF, the likelihood of finding a source serendipitously at a suitable position is about $K = 50/(1''/0''.060)^2 = 0.18$. To meet these conditions independently for 12 times, the likelihood is $K^{12} = 1.2 \times 10^{-9}$, which is too small to be considered.

Appendix C Reidentification of S62

Here, the primary goal is to show that, despite the complex field, S62 could be reidentified while S2 is approaching its periape position. S62 is showing very little proper motion because of its apoaapse position, while all other sources in the crowded field move. Shortly before pericenter passage of S2 in 2018.37, the star passed through the S62 orbit as S62 was approaching its apocenter position. In 2014–2016, it was basically impossible to measure S62 due to the presence of the $K = 14$ bright star S2. However, S62 could be reidentified in the crowded region between 2017 and 2019. Due to its high eccentricity of around 0.97, the S62 orbit is precisely determined and the position of the apocenter and the time for the apocenter passage are well known. For the sources close to S62, their trajectories could be calculated by performing orbital fits to the NACO data covering the years 2002–2018. We also adapted the data presented in Do et al. (2019).

In Figure 10 we show the source arrangement in the years 2017, 2018, and 2019 close to the S62 apocenter position. For 2017 and 2018, we used the single best NACO data set (see Tables 3 and 4), which allowed high angular resolution imaging in the region around SgrA*. For 2019, we show a Gaussian model representing the source distribution published by Do et al. (2019) in their Figure 2. Comparison of the images with the resulting orbital calculations (see Table 6) allows us to reidentify S62. In Figure 10, we show relevant S-stars in the region just west of SgrA*: S19, S29, S38, S42, S60, and S64. We also indicate S23, S31, S56, and S63 in some years.

In 2018, S62 seems to be fainter. It should be noted that high-resolution observations result in high-sensitivity images. Sources in a crowded field are not constantly bright as a function of time (i.e., from year to year). This is due to the varying AO performance, the signal-to-noise, and most of all due to the variable background. As shown by Sabha et al. (2012), significant variations on timescales of 1–3 yr can be expected for fainter sources in the GC.

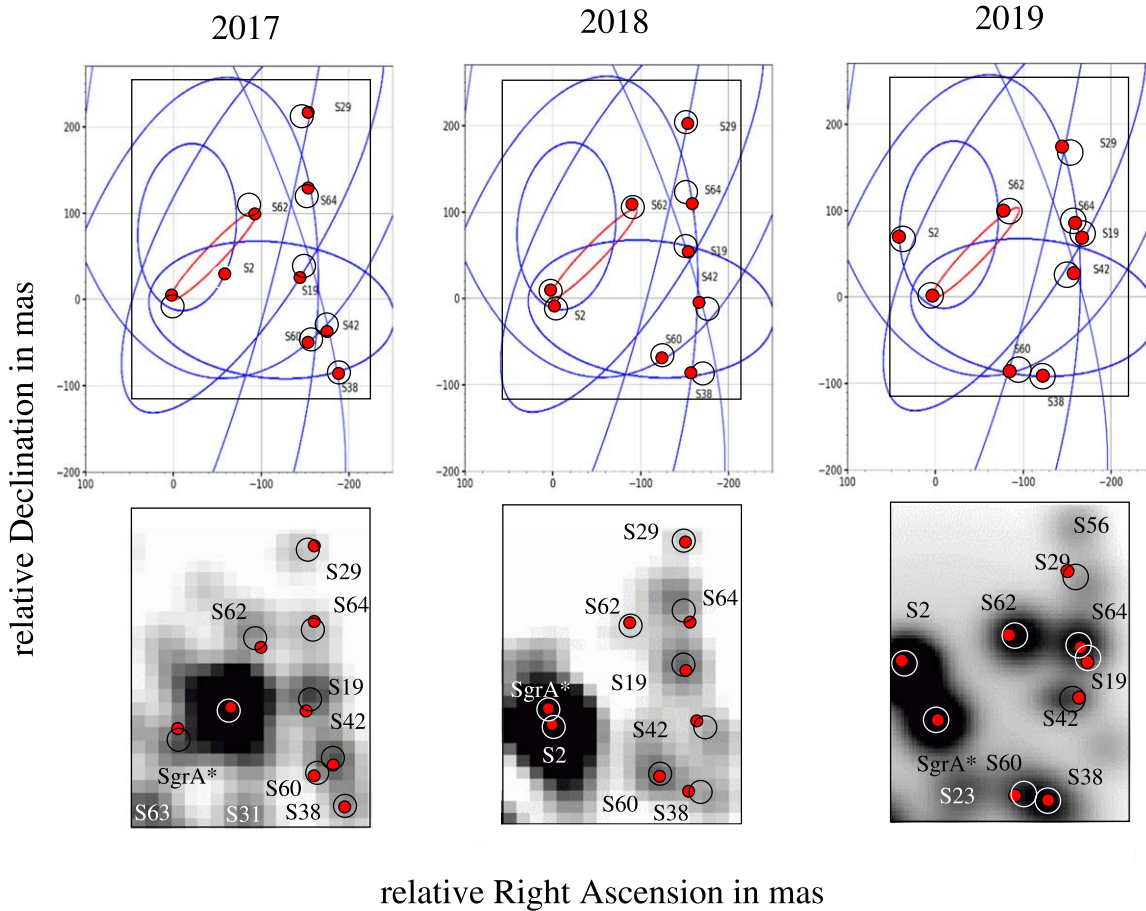


Figure 10. Reidentification of S62 after S2 passed through the FOV in 2014–2016. We clearly detect the star S62 in 2017, 2018, and 2019. Top: predictions from orbital calculations based on data from 2002 until 2019 (see the text for details). Bottom: single-epoch images at the diffraction limit. The description of the symbols is given in the text. The image scales in the top panels are given in milliarcseconds. The rectangle in the top panels outlines the FOV circumference of the lower panels.

Table 6
Orbital Elements of the Indicated Stars of Figure 10

Star	$a(\text{mpc})$	e	$i(^{\circ})$	$\omega(^{\circ})$	$\Omega(^{\circ})$	$t_{\text{closest}}(\text{yr})$
S2	5.04 ± 0.01	0.884 ± 0.002	136.88 ± 0.40	71.33 ± 0.75	234.51 ± 1.03	2002.32 ± 0.02
S19	11.52 ± 1.98	0.606 ± 0.073	69.67 ± 2.96	139.00 ± 5.96	335.64 ± 2.58	2004.48 ± 0.01
S29	28.69 ± 2.55	0.476 ± 0.095	101.64 ± 2.01	350.70 ± 13.26	170.00 ± 2.07	2046.98 ± 4.89
S38	5.63 ± 0.21	0.804 ± 0.050	159.86 ± 15.01	15.70 ± 9.65	98.43 ± 8.31	2003.33 ± 0.34
S42	38.60 ± 2.75	0.649 ± 0.041	65.43 ± 0.91	39.89 ± 2.87	206.32 ± 2.24	2012.29 ± 1.39
S60	20.37 ± 3.22	0.833 ± 0.087	132.43 ± 6.42	50.31 ± 19.69	206.40 ± 24.07	2021.50 ± 4.99
S62	3.59 ± 0.01	0.976 ± 0.002	72.76 ± 4.68	42.62 ± 0.40	122.61 ± 0.57	2003.33 ± 0.01
S64	15.90 ± 2.71	0.354 ± 0.126	114.21 ± 1.80	155.11 ± 31.35	167.11 ± 8.75	2005.56 ± 5.27

In 2017, the Lucy image reconstruction is difficult since S2 is very close to S62 and the neighboring sources to the west. Also, the region toward S64 appears to be distorted. The red circles indicate the predicted positions of the sources. The red circles have a width of ± 6.5 mas corresponding to the nominal uncertainty we reached for S62 (see Table 2) based on several position measurements per epoch. The comparison between the predicted positions and the single-epoch images in Figure 10 is hampered by (1) the uncertainties in the orbital elements and (2) by the scatter in the single-epoch results depending on the line-of-sight background and the immediate vicinity of the sources. The black circles have a width of ± 13 mas

corresponding to ± 1 pixel (i.e., \pm one fifth of a diffraction limited beam) for the NACO camera in the K band (see also the discussion in Appendix B). They are centered between the expected position and the actual peak position obtained for the single-epoch image representation of the field.

Appendix D SINFONI K -band Images of the GC

Here, we present the K_S -band images (Figure 11) that have been extracted from the SINFONI data cubes. The on-source integration 210 minutes for 2008, 640 minutes for 2010, and 610 minutes for 2012.

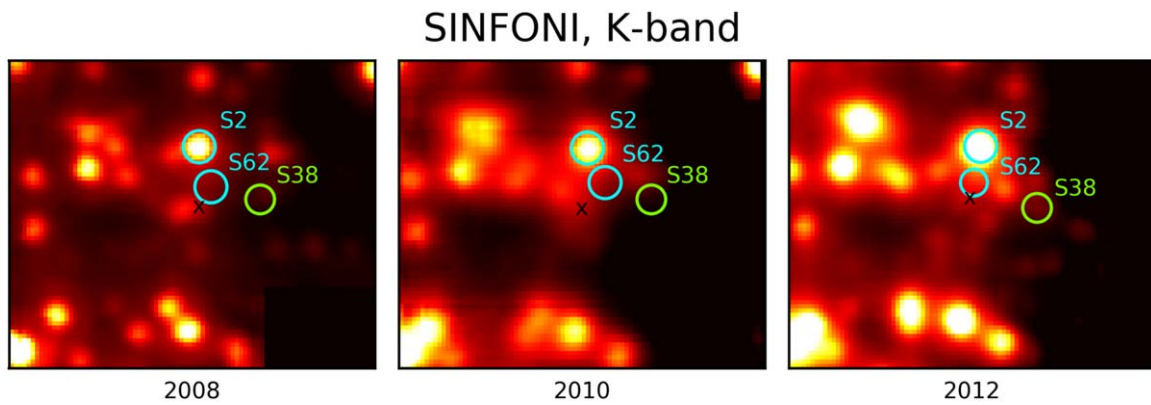


Figure 11. *K*-band images of the GC extracted from the collapsed SINFONI data cubes. No Lucy–Richardson algorithm or spatial frequency filters have been applied to these images (see also the caption of Figure 1).

We shifted the marked S2 star to a fixed position. SgrA* is marked with a black *x*.

Appendix E PSF Subtraction

Here, we demonstrate that the successful detection of the star S62 is not an artifact of the deconvolution process. Furthermore, the source can be detected by subtracting bright

sources in its vicinity. In Figure 12, we show the results of the PSF subtraction. As shown, we subtracted several PSFs scaled to the brightness of surrounding stars in order to highlight the presence of S62. We use images from 2008, 2010, and 2012 as examples. The NACO *K*-band images with all stars are aligned in the first row. The second row shows the detection of S62 after the subtraction of the nearby stars. The bright star close to the center is S2. Additional stars are labeled in Figures 1, 3, 4, and 11.

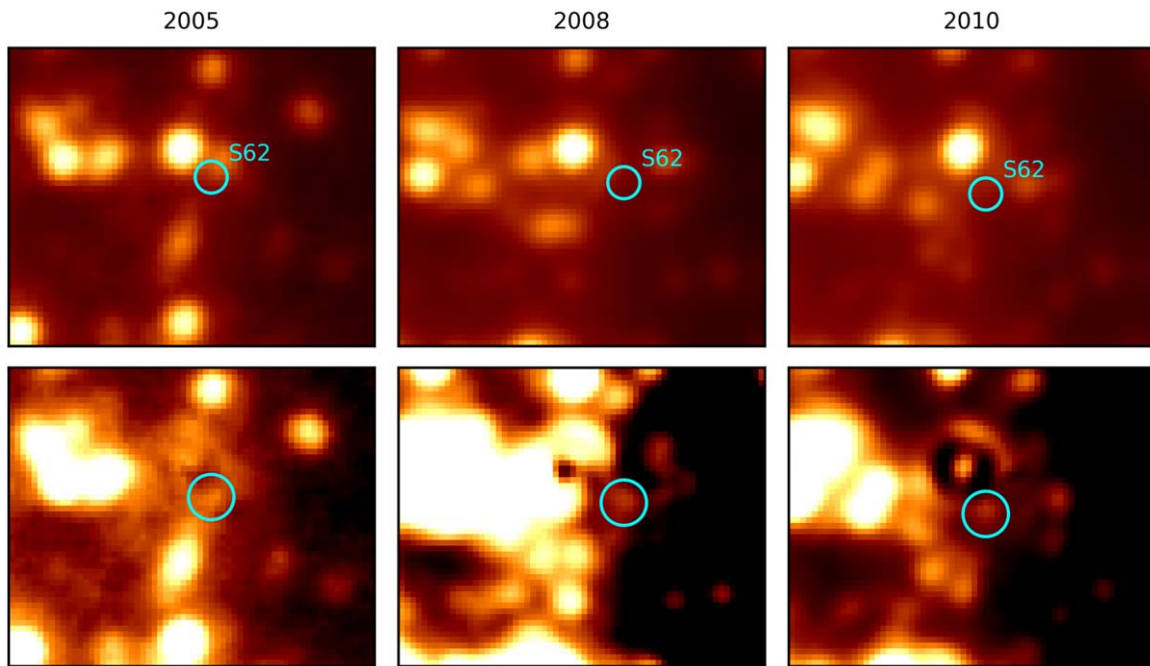


Figure 12. Galactic center in 2005, 2008, and 2010. North is up and east is to the left. The upper three NACO *K*-band images have been taken with the S13 camera (13 mas/spatial pixel scale) and show the S-cluster without any subtracted star. S62 is indicated by a cyan circle. The lower three images show the PSF-subtracted results in the corresponding years. The circle is at the same position and shows the source S62 at the same position as in the corresponding deconvolved images in Figure 2.

ORCID iDs

Florian Peißker  <https://orcid.org/0000-0002-9850-2708>
 Andreas Eckart  <https://orcid.org/0000-0001-6049-3132>

References

- Alexander, T. 2017, *ARA&A*, **55**, 17
 Benz, W., & Hills, J. G. 1987, *ApJ*, **323**, 614
 Boehle, A., Ghez, A. M., Schödel, R., et al. 2016, *ApJ*, **830**, 17
 Cai, R.-G., Liu, T.-B., & Wang, S.-J. 2018, arXiv:1808.03164
 Davies, R. I. 2007, *MNRAS*, **375**, 1099
 Demircan, O., & Kahraman, G. 1991, *Ap&SS*, **181**, 313
 Do, T., Witzel, G., Gautam, A. K., et al. 2019, *ApJL*, **882**, L27
 Eckart, A., Britzen, S., Horrobin, M., et al. 2013, arXiv:1311.2743
 Eckart, A., & Genzel, R. 1996, *Natur*, **383**, 415
 Eckart, A., & Genzel, R. 1997, *MNRAS*, **284**, 576
 Eckart, A., Genzel, R., Ott, T., & Schödel, R. 2002, *MNRAS*, **331**, 917
 Eckart, A., Hüttemann, A., Kiefer, C., et al. 2017, *FoPh*, **47**, 553
 Eckart, A., Muzić, K., Yazıcı, S., et al. 2013, *A&A*, **551**, A18
 Eisenhauer, F., Abuter, R., Bickert, K., et al. 2003, *Proc. SPIE*, **4841**, 1548
 Fragione, G., Leigh, N. W. C., Perma, R., & Kocsis, B. 2019, *MNRAS*, **489**, 727
 Gaburov, E., Lombardi, J. C., Jr., & Portegies Zwart, S. 2010, *MNRAS*, **402**, 105
 Genzel, R., Eisenhauer, F., & Gillessen, S. 2010, *RvMP*, **82**, 3121
 Ghez, A. M., Duchene, G., Morris, M., et al. 2002, AAS Meeting Abstracts, **201**, 68.04
 Ghez, A. M., Klein, B. L., Morris, M., & Becklin, E. E. 1998, *ApJ*, **509**, 678
 Gillessen, S., Eisenhauer, F., Fritz, T. K., et al. 2009a, *ApJL*, **707**, L114
 Gillessen, S., Eisenhauer, F., Trippe, S., et al. 2009b, *ApJ*, **692**, 1075
 Gillessen, S., Plewa, P. M., Eisenhauer, F., et al. 2017, *ApJ*, **837**, 30
 Gravity Collaboration, Abuter, R., Accardo, M., et al. 2017, *A&A*, **602**, A94
 Gravity Collaboration, Abuter, R., Amorim, A., et al. 2018a, *A&A*, **615**, L15
 Gravity Collaboration, Abuter, R., Amorim, A., et al. 2018b, *A&A*, **618**, L10
 Gravity Collaboration, Abuter, R., Amorim, A., et al. 2019, *A&A*, **625**, L10
 Hills, J. G. 1988, *Natur*, **331**, 687
 Horrobin, M., Eisenhauer, F., Tecza, M., et al. 2004, *AN*, **325**, 88
 Jalali, B., Pelupessy, F. I., Eckart, A., et al. 2014, *MNRAS*, **444**, 1205
 Karssen, G. D., Bursa, M., Eckart, A., et al. 2017, *MNRAS*, **472**, 4422
 Krabbe, A., Genzel, R., Eckart, A., et al. 1995, *ApJL*, **447**, L95
 Lenzen, R., Hartung, M., Brandner, W., et al. 2003, *Proc. SPIE*, **4841**, 944
 Lucy, L. B. 1974, *AJ*, **79**, 745
 Meyer, F., & Meyer-Hofmeister, E. 2012, *A&A*, **546**, L2
 Ott, T., Eckart, A., & Genzel, R. 1999, *ApJ*, **523**, 248
 Parsa, M., Eckart, A., Shahzamanian, B., et al. 2017, *ApJ*, **845**, 22
 Peißker, F., Zajaček, M., Eckart, A., et al. 2019, *A&A*, **624**, A97
 Rasskazov, A., Fragione, G., Leigh, N. W. C., et al. 2019, *ApJ*, **878**, 17
 Richardson, W. H. 1972, *JOSA*, **62**, 55
 Rousset, G., Lacombe, F., Puget, P., et al. 2003, *Proc. SPIE*, **4839**, 140
 Sabha, N., Eckart, A., Merritt, D., et al. 2012, *A&A*, **545**, A70
 Saputro, D. R. S., & Widyaningsih, P. 2017, AIP Conf. Proc. 1868, The 4TH Int. Conf. on Research, Implementation, and Education of Mathematics and Science, **040009**
 Sari, R., & Fragione, G. 2019, arXiv:1907.03312
 Schödel, R., Ott, T., Genzel, R., et al. 2002, *Natur*, **419**, 694
 Shahzamanian, B., Eckart, A., Zajaček, M., et al. 2016, *A&A*, **593**, A131
 Trac, H., Sills, A., & Pen, U.-L. 2007, *MNRAS*, **377**, 997
 Weinberg, S. 1972, Gravitation and Cosmology: Principles and Applications of the General Theory of Relativity (New York: Wiley)
 Witzel, G., Eckart, A., Bremer, M., et al. 2012, *ApJS*, **203**, 18
 Wollman, E. R., Geballe, T. R., Lacy, J. H., Townes, C. H., & Rank, D. M. 1977, *ApJL*, **218**, L103